Body Wave Separation in the Time-Frequency Domain

Roberto H. Herrera, *Member, IEEE*, Jean Baptiste Tary, Mirko van der Baan, and David W. Eaton

***Abstract*—Separation of a seismogram into its individual constitutive phases (P- and S-wave arrivals, surface waves, etc.) is a long-standing problem. In this letter, we use a high-resolution time-frequency transform to achieve this and reconstruct their individual waveforms in the time domain. The procedure is illustrated using microseismic events recorded during a hydraulic fracturing treatment. The synchrosqueezing transform is an extension of the continuous wavelet transform combined with frequency reassignment. Its high-resolution time-frequency decompositions allow for separation and identification of P- and S-waves with subtly different frequency contents that would not be recoverable using short-term Fourier transforms due to its smearing in the frequency domain. It is an invertible transform, thus allowing for signal reconstruction in the time domain after signal separation. The same approach is applicable to other seismic signals such as resonance frequencies and long-period events and offers promising new possibilities for enhanced signal interpretation in terms of underlying physical processes.**

***Index Terms*—Signal reconstruction, spectral decomposition, synchrosqueezing transform (SST), wave separation.**

I. Introduction

THE separation of P- and S-waves is a challenging task that, if solved, could bring more insights into the nature and location of the generating source. It is crucial in estimating the subsurface elastic properties (e.g., [1]–[5]), which can later be used, for instance, in moment tensor inversion [6], [7] or improved event locations [8], [9].

The problem of separating P- and S-waves was addressed by Dankbaar [10], with the application of a filter in the wavenumber–frequency domain to remove the array's response from the incident wavefield. The filter coefficients are extracted from the near-surface P- and S-wave velocity and from the geometry of the geophone groups. It can also be done by divergence and curl computations in the space domain [11], [12]. These wave-theoretical methods rely on the complete characterization of the wave propagation field [13], which requires dense arrays of receivers situated inside a thin homogeneous layer [2], [10], [11].

Alternative parametric methods, e.g., [14] and [15], on the other hand, do not require *a priori* information about the near-surface layer, but they assume that the signal is comprised only of a small number of interfering plane waves [11]. Thus, these methods cannot handle more complex wave propagation phenomena, e.g., the free-surface effect [13]. Statistical approaches, like independent component analysis [13], exploit the statistical differences between the P- and S-waves without the need of further *a priori* information but are limited to cases where the wave components are statistically independent.

Time-frequency analysis is an alternative choice, specifically if signal components separate in the time domain or the frequency domain. In the first case, simple time domain tapering can retrieve the signals. In the other case, bandpass filtering is sufficient. Alternatively, short-time Fourier transforms (STFTs) or continuous wavelet transforms (CWTs) can retrieve the signal components if they do not overlap in the time-frequency domain [16]–[18] and if the invoked transform has sufficiently high time-frequency resolution. Indeed, each transform introduces temporal and spectral smearing [19] which may impede successful separation even if the original components do not overlap.

We present a derivative of the CWT, called synchrosqueezing, that improves the resolution of the time-frequency map via a combination of frequency-reassignment [20] with instantaneous frequency (IF) estimation [21]. We first introduce the theory of the synchrosqueezing transform (SST) and then test our method on two microseismic events from a hydraulic fracturing treatment [22].

II. Theory

We represent a time domain seismic signal $s(t)$ in terms of time-varying harmonic components K [19], [21]

$$s(t) = \sum_{k=1}^{K} A_k(t) \cos\left(\theta_k(t)\right) + \eta(t) \tag{1}$$

where $A_k(t)$ is the instantaneous amplitude and $f_k(t) = (1/2\pi)(d/dt)\theta_k(t)$ is the IF of the signal component k, derived from the instantaneous phase $\theta_k(t)$. $\eta(t)$ represents the additive noise.

Daubechies *et al.* [21] noticed that the CWT of the signal $s(t)$ could be improved by computing the IF of the wavelet coefficients followed by a frequency reassignment step. An application to seismic signal processing with extended theory can be found in [19]. The transformation starts from the CWT of signal $s(t)$ [23]

$$W_s(a,b) = \frac{1}{\sqrt{a}} \int s(t) \psi^* \left(\frac{t-b}{a} \right) dt \tag{2}$$

Manuscript received April 30, 2014; revised June 27, 2014; accepted July 17, 2014. Date of publication August 12, 2014; date of current version August 21, 2014.

R. H. Herrera was with the Department of Physics, University of Alberta, Edmonton, AB T6G 2E1, Canada. He is now with UT Technology, Edmonton, AB T6P 1N5, Canada (e-mail: henryherrera@ieee.org).

J. B. Tary was with the Department of Physics, University of Alberta, Edmonton, AB T6G 2E1, Canada. He is now with the Department of Meteorology and Geophysics, University of Vienna, 1090 Vienna, Austria.

M. van der Baan is with the Department of Physics, University of Alberta, Edmonton, AB T6G 2E1, Canada.

D. W. Eaton is with the Department of Geoscience, University of Calgary, Calgary, AB T2N 1N4, Canada.

Digital Object Identifier 10.1109/LGRS.2014.2342033

where ψ^* is the complex conjugate of the mother wavelet and b is the translation of the mother wavelet which is also scaled by a. $W_s(a,b)$ are the coefficients which are used to compute the IFs $\omega_s(a,b)$ [21]

$$\omega_s(a,b) = \frac{-j}{W_s(a,b)} \frac{\partial W_s(a,b)}{\partial b}. \tag{3}$$

The final reassignment step maps every point (b,a) to $(b,\omega_s(a,b))$. This combination of CWT and IF followed by reassignment of the wavelet coefficients is called synchrosqueezing [21]. We can compute the discrete scale $\Delta a_k = a_{k-1} - a_k$ for any a_k in the wavelet coefficient matrix $W_s(a,b)$. When mapping from the time-scale plane to the time-frequency plane $(b,a) \rightarrow (b, w_s(a,b))$, the SST $T_s(w,b)$ is determined only at the centers ω_l of the frequency range $[\omega_l - \Delta\omega/2, \omega_l + \Delta\omega/2]$, with $\Delta\omega = \omega_l - \omega_{l-1}$

$$T_s(\omega_l, b) = \frac{1}{\Delta\omega} \sum_{a_k : |\omega(a_k,b) - \omega_l| \leq \Delta\omega/2} W_s(a_k, b) a^{-3/2} \Delta a_k. \tag{4}$$

From the discrete version of the SST $\tilde{T}_s(\omega_l, t_m)$, with discrete time $t_m = t_0 + m\Delta t$ at a sampling rate Δt, we can reconstruct the individual components over a small frequency band $l \epsilon L_k(t_m)$ around the kth component [24]

$$s_k(t_m) = 2C_\phi^{-1} \Re \left(\sum_{l \epsilon L_k(t_m)} \tilde{T}_{\tilde{s}}(w_l, t_m) \right) \tag{5}$$

where C_ϕ is a constant dependent on the selected wavelet. As we take the real part $\Re$ of the discrete SST in that band, we recover the real component s_k. An extended explanation can be found in [24] with applications to seismic signals in [19].

III. Applications to Microseismic Signals

A. Event 1: Time-Frequency Representation and Polarization

Fluid injection during hydraulic fracturing of tight reservoir generates multiple brittle failure events inside the reservoir [25]. Arrival times of body waves generated by these small magnitude events $(-3 < M_w < -1)$ are usually very close, and their limited bandwidth can cause even partial overlap in the time and frequency domains.

The data set used in our example comes from multistage hydraulic fracturing treatment programs performed in two horizontal wells (see [22] for more details). Six 3C geophones with a sampling rate of 0.5 ms were deployed in a deviated borehole.

Event 1 is recorded by the vertical component of the deepest geophone at well A stage 2 [Fig. 1(a)]. P- and S-waves are visible in the time domain signal. Fig. 1(b) shows the STFT spectra for the signal segment from 0.2 to 0.7 s and frequencies from 100 to 400 Hz. We use a Hanning window of 64 ms with 50% overlap. The frequency components are blurred in the time-frequency representation due to the limited resolution of this transform. For the SST, we use a bump wavelet with a ratio central frequency to bandwidth of 50 and 32 intermediate

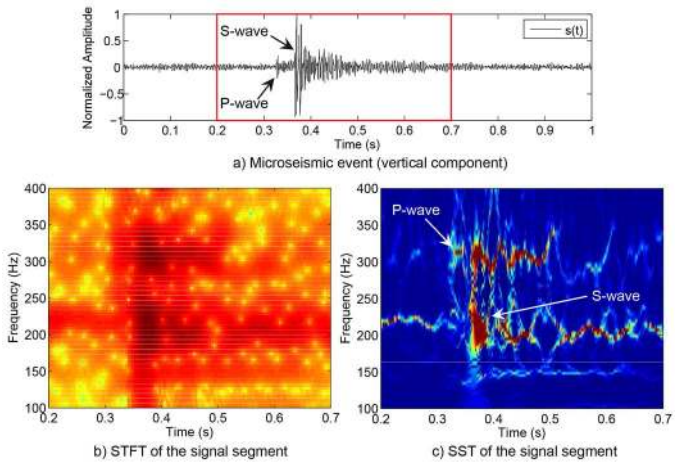

Fig. 1. Event 1. (a) Microseismic event (vertical component). (b) STFT for the segment of the signal shown in (a) by the red rectangle. (c) SST output for the same portion.

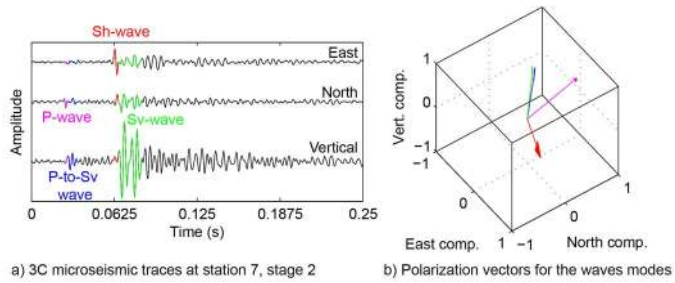

Fig. 2. 3C time series for event 1 (left) and eigenvectors estimated from their hodograms. Colors indicate possible wave types for each wavepacket. (a) 3C microseismic traces at station 7, stage 2. (b) Polarization vectors for the waves modes.

scales per octave. The SST produces a sharper time-frequency representation [Fig. 1(c)] showing frequency components that are hidden in the STFT.

In a single-component trace as in Fig. 1(c), it is not immediately clear which frequency component belongs to which wave. We apply a polarization analysis on all three components to identify individual P- and S-wave arrivals and project them onto their main components.

Using the classical covariance matrix method [26], we find the main axes for the three eigenvectors. No satisfactory set of orthogonal vectors is obtained by the classical decomposition in radial, transverse, and pseudovertical components, mostly due to the waves having nonlinear polarizations. We first isolate each wavepacket and then compute the principal eigenvector from the 3C signal. The resulting set of vectors for the 3C signal from Fig. 2(a) is presented in Fig. 3(b) and shows quasi-orthogonal polarizations. The North component shows the most prominent P-wave arrival (magenta). The converted P- to S-wave (blue) follows the main P-wave and has almost the same polarization as the Sv-wave (green). The Sh-wave (red) clearly visible in the East component is close to orthogonal to the P- and Sv-waves.

Fig. 4 shows the 3C data projected onto its eigenvectors and their time-frequency representations using the SST and the STFT. Despite the 3C data projection, some energy of the

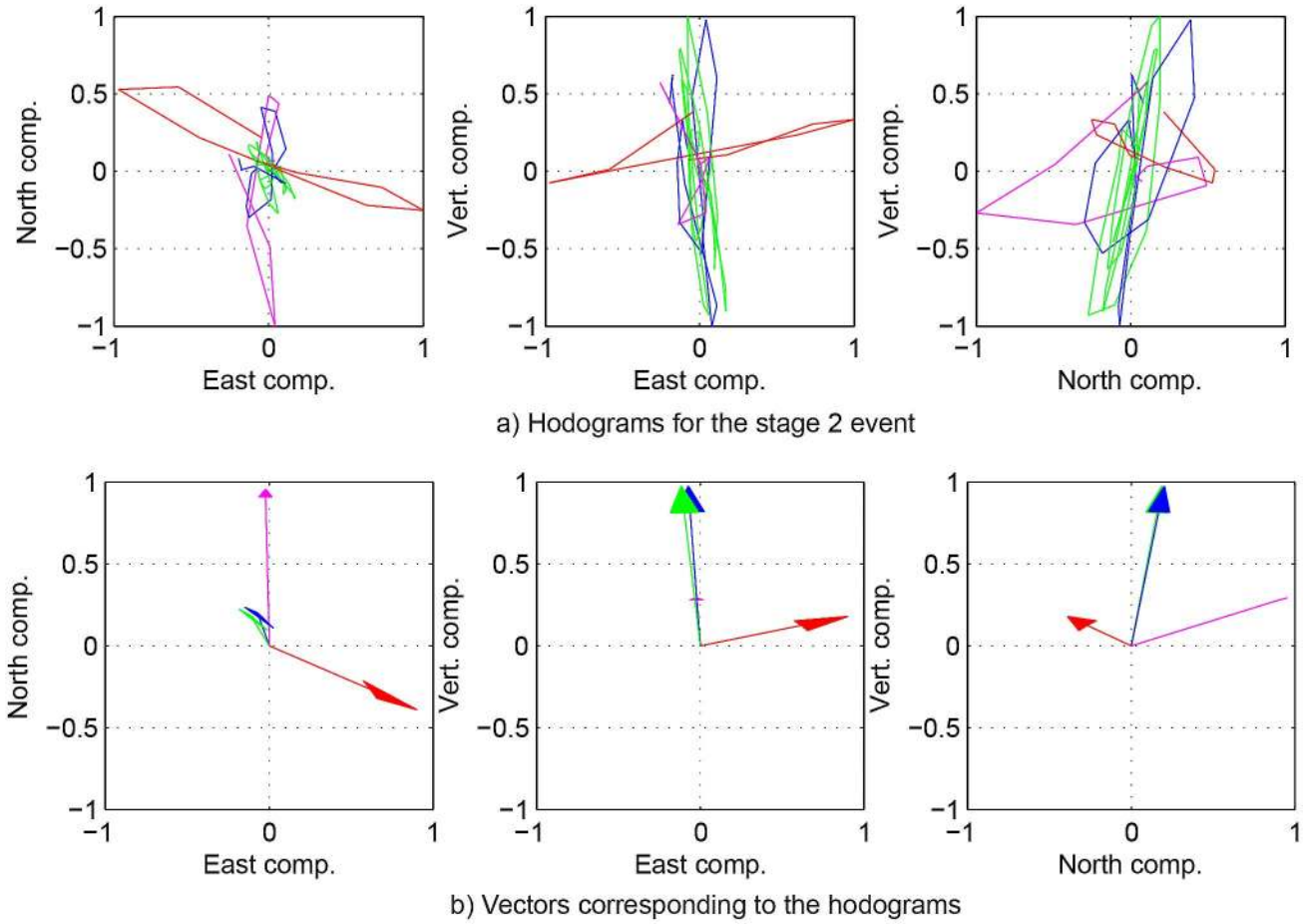

Fig. 3. Hodograms and corresponding vectors for the three components shown in Fig. 2. (a) Hodograms for the stage 2 event. (b) Vectors corresponding to the hodograms.

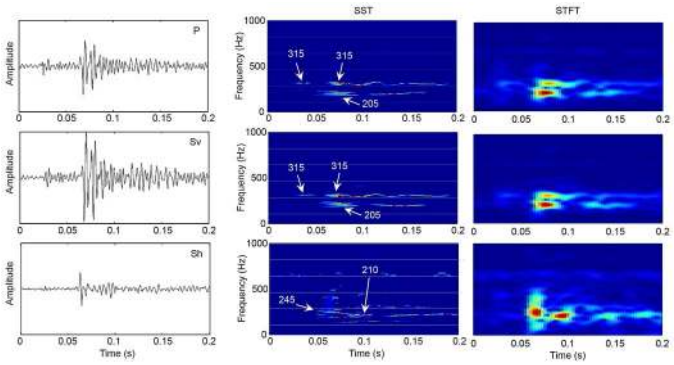

Fig. 4. Event 1: projected components and their corresponding time-frequency representations using SST and STFT. The STFT is computed using a Hanning window of 0.03 s and 90% overlap. The amplitude scale of the three components is normalized by the maximum amplitude of the strongest eigenvector. The main spectral components are highlighted on the SST plot with arrows and their corresponding values.

different wavepackets may leak onto other components due to their nonlinear polarizations. The central frequency of the P-wave appears to be about 315 Hz. The Sv-wave projection shows the P-to-Sv-wave around 0.05 s with a frequency at 315 Hz, and then, the Sv-wave splits into two components at 205 and 315 Hz. The Sh-wave projection shows two strong components of 245 and 210 Hz.

The enhanced resolution of the SST permits recognition of the various phases present in the three-component recording which would not have been possible using an STFT, although a comparison of Fig. 1(b) and (c) indeed confirms their presence in both time-frequency representations even if, in the STFT, the phases are blurred. Next, we show a second example and illustrate the waveform reconstruction in the time domain after separation.

B. Event 2: Time-Frequency Decomposition and Signal Reconstruction

Next, we use another microseismic event from this experiment. Fig. 5 shows the three-component seismogram for event 2. The vertical component shows the most prominent P-wave (magenta). As before, we separate the seismograms into three signals with quasi-orthogonal polarization, namely, P-, Sv-, and Sh-waves. Fig. 6 shows their projections onto the eigenvectors. The P-wave projection has a central frequency around 280 Hz. Sv-wave contributions are around 305 Hz. The patch at 320 Hz on the Sv-wave projection corresponds to the arrival time of the P-wave. It could then also be contributions of the remnant P-wave broadband spectrum projected onto the Sv-component due to its nonlinear polarization. The Sh-wave projection shows two strong components at 290 and 350 Hz. There is a patch at 185–225 Hz present in all components.

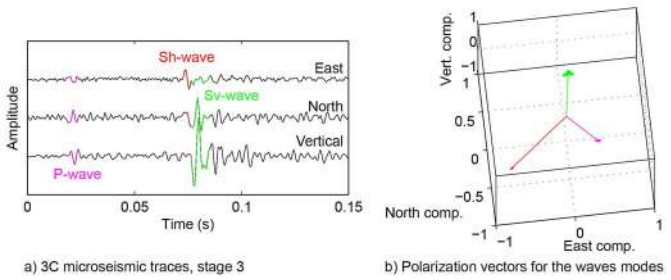

Fig. 5. Three-component seismogram (left) and corresponding hodograms (right) for event 2. Colors indicate possible wave types for each wavepacket. The three phases P, Sv, and Sh are quasi-perpendicular. (a) 3C microseismic traces, stage 3. (b) Polarization vectors for the waves modes.

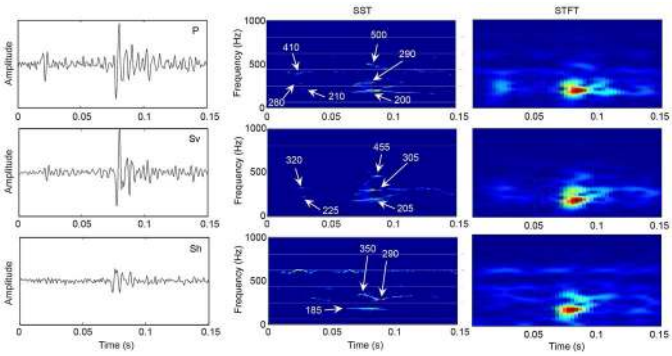

Fig. 6. Event 2: projected components and their corresponding time-frequency representations using SST and STFT. The STFT is computed using a Hanning window of 0.03 s and 90% overlap. The amplitude scale of the three components is normalized by the maximum amplitude of the strongest eigenvector. The main spectral components are highlighted on the SST plot with arrows and their corresponding values.

Time domain reconstruction is possible by extracting a vertical rectangle comprising only the P- or S-waves in the time-frequency domain and applying an inverse SST following (5) (Fig. 7). The reconstructed phases in red resemble the original signals (blue), which include all of the frequency bands in the same time segment. In this case, both waves are separated in the time domain, yet such a narrow time-frequency filtering operation would be more challenging for the corresponding STFT decompositions due to its increased spectral smearing (Fig. 6).

IV. Discussion

Both events show an interesting pattern with P- and S-waves comprising consistently two to three narrow-band frequency components. The band-limited nature of microseismic signals imposes another degree of complexity on separating frequency components. For both examples, polarization analysis clearly shows a quasi-orthogonal set of three to four wavepackets arriving at the receivers. For the first example, the P-wave is immediately followed by another wave with a polarization similar to the principal Sv-wave. The frequency content of seismic waves is not expected to change due to body wave conversion when incidence angles remain real-valued [27] but arise at the source [28] or due to frequency-dependent attenuation and wave scattering [29]–[31]. A tentative interpretation of the series of arrivals for the first example could be as

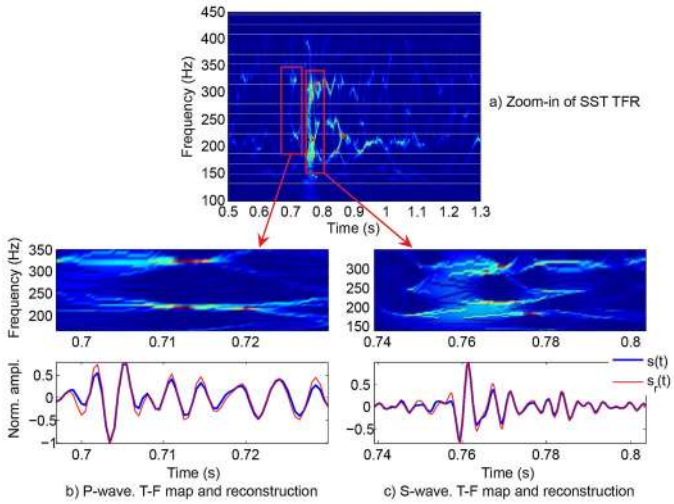

Fig. 7. Time domain reconstruction of the P- and S-waves. The reconstructed waveform (red) shows good approximation with the original component (blue). (a) Zoom-in of SST TFR. (b) P-wave. T-F map and reconstruction. (c) S-wave. T-F map and reconstruction.

follows. The P-wave with a frequency content around 315 Hz is converted to an Sv-wave close to the receiver location, leading to a change in polarization but no frequency changes. Then, Sh- and Sv-waves arrive with a frequency content around 245 and 205 Hz, respectively. The second component at 315 Hz could correspond to a P-wave converted close to the source location.

At this stage of the analysis, multiple explanations are possible. Some noises appearing as spectral lines are visible on the SST representations, showing potential flaws in the instrument clamping. Some of the monofrequency components of the observed body waves could then correspond to the instrument response to the microseismic excitation. Most of the S-wave frequency components also have relatively long-duration monofrequency tails, which could also arise from ringing due to bad coupling. The analysis of the recordings at other geophones, including other events as well, may help in assessing the impact of the instruments on the recorded data [32].

Another interesting possibility is that the two frequency contents originate from two concomitant processes at the source location creating different signals. For instance, a shear failure event on one fracture could be accompanied by tensile failure on a wing fracture, or one P-wave and two S-wave radiation lobes could be indicative of a compensated linear vector dipole fracture type [33]. Nondouble couple events indeed play an important role in rock deformation during hydraulic fracturing [22], [34].

Irrespective of the cause of the detected narrow-band signals, SST allows for separation of these waves in the time-frequency plane and subsequent time domain reconstruction after high-resolution filtering. This would be challenging for many other time-frequency transforms due to their associated temporal and spectral smearing.

In addition to SST, several other high-resolution time-frequency transforms exist such as empirical mode decomposition [35], [36] and nonstationary autoregressive models [37].

These methods are based on very different concepts from wavelet and Fourier transforms yet remain reversible such that they offer much promise for seismic data processing and interpretation.

V. Conclusion

The increased resolution of the SST and variants in the time-frequency plane provides useful information that was hitherto hidden by traditional methods. We have illustrated its use for identification and separation of narrow-band P- and S-waves for two microseismic events. The proposed method works even if the different phases overlap in time yet separated by their frequency content. We have envisioned various applications for SST and other high-resolution transforms including improved event detection, identification and location, time picking, wavefield separation, and possibly moment tensor inversions.

Acknowledgment

The authors would like to thank S. Fomel for the encouraging discussions about the use of SST for P- and S-wave separation, M. Grob and S. Maxwell for the interesting suggestions on the interpretation side, and Thakur *et al.* [24] for making the SST toolbox available.

References

[1] F. Scherbaum, "Combined inversion for the three-dimensional Q structure and source parameters using microearthquake spectra," *J. Geophys. Res.*, vol. 95, no. B8, pp. 12 423–12 438, Aug. 1990.

[2] Y. Wang, S. C. Singh, and P. J. Barton, "Separation of P- and SV-wavefields from multi-component seismic data in the $\tau - \mathrm{p}$ domain," *Geophys. J. Int.*, vol. 151, no. 2, pp. 663–672, Nov. 2002.

[3] B. P. Allmann, P. M. Shearer, and E. Hauksson, "Spectral discrimination between quarry blasts and earthquakes in Southern California," *Bull. Seismol. Soc. Amer.*, vol. 98, no. 4, pp. 2073–2079, Aug. 2008.

[4] B. A. Chouet and R. S. Matoza, "A multi-decadal view of seismic methods for detecting precursors of magma movement and eruption," *J. Volcanol. Geotherm. Res.*, vol. 252, pp. 108–175, Feb. 2013.

[5] P. Lesage, F. Glangeaud, and J. Mars, "Applications of autoregressive models and time-frequency analysis to the study of volcanic tremor and long-period events," *J. Volcanol. Geotherm. Res.*, vol. 114, no. 3/4, pp. 391–417, May 2002.

[6] V. Vavryčuk and D. Kühn, "Moment tensor inversion of waveforms: A two-step time-frequency approach," *Geophys. J. Int.*, vol. 190, no. 3, pp. 1761–1776, Sep. 2012.

[7] A. D. Miller, B. R. Julian, and G. R. Foulger, "Three-dimensional seismic structure and moment tensors of non-double-couple earthquakes at the Hengill-Grensdalur volcanic complex, Iceland," *Geophys. J. Int.*, vol. 133, no. 2, pp. 309–325, May 1998.

[8] C. Ji, D. J. Wald, and D. V. Helmberger, "Source Description of the 1999 Hector Mine, California, Earthquake Part I: Wavelet Domain Inversion Theory and Resolution Analysis," *Bull. Seismol. Soc. Amer.*, vol. 92, no. 4, pp. 1192–1207, May 2002.

[9] D. Fagan, K. van Wijk, and J. Rutledge, "Clustering revisited: A spectral analysis of microseismic events," *Geophysics*, vol. 78, no. 2, pp. KS41–KS49, Mar. 2013.

[10] J. W. M. Dankbaar, "Separation of P- and S-waves," *Geophys. Prospect.*, vol. 33, no. 7, pp. 970–986, Nov. 1985.

[11] J. O. A. Robertsson and A. Curtis, "Wavefield separation using densely deployed three-component single-sensor groups in land surface-seismic recordings," *Geophysics*, vol. 67, no. 5, pp. 1624–1633, Sep. 2002.

[12] R. Sun, G. A. McMechan, H. Hsiao, and J. Chow, "Separating P- and S-waves in prestack 3D elastic seismograms using divergence and curl," *Geophysics*, vol. 69, no. 1, pp. 286–297, Jan. 2004.

[13] M. Van der Baan, "PP/PS wavefield separation by independent component analysis," *Geophys. J. Int.*, vol. 166, no. 1, pp. 339–348, Jul. 2006.

[14] C. Esmersoy, "Inversion of P and SV waves from multicomponent offset vertical seismic profiles," *Geophysics*, vol. 55, no. 1, pp. 39–50, Jan. 1990.

[15] W. H. Cho and T. W. Spencer, "Estimation of polarization and slowness in mixed wavefields," *Geophysics*, vol. 57, no. 6, pp. 805–814, Jun. 1992.

[16] A. Roueff, J. Chanussot, J. I. Mars, and M.-Q. Nguyen, "Unsupervised separation of seismic waves using the watershed algorithm on time-scale images," *Geophys. Prospect.*, vol. 52, no. 4, pp. 287–300, Jul. 2004.

[17] M. Diallo, M. Kulesh, M. Holschneider, and F. Scherbaum, "Instantaneous polarization attributes in the time-frequency domain and wavefield separation," *Geophys. Prospect.*, vol. 53, no. 5, pp. 723–731, Sep. 2005.

[18] M. Kulesh *et al.*, "Polarization analysis in the wavelet domain based on the adaptive covariance method," *Geophys. J. Int.*, vol. 170, no. 2, pp. 667–678, Aug. 2007.

[19] R. H. Herrera, J. Han, and M. van der Baan, "Applications of the synchrosqueezing transform in seismic time-frequency analysis," *Geophysics*, vol. 79, no. 3, pp. V55–V64, May 2014.

[20] P. Flandrin, G. Rilling, and P. Goncalves, "Empirical mode decomposition as a filter bank," *IEEE Signal Process. Lett.*, vol. 11, no. 2, pp. 112–114, Feb. 2004.

[21] I. Daubechies, J. Lu, and H.-T. Wu, "Synchrosqueezed wavelet transforms: An empirical mode decomposition-like tool," *Appl. Comput. Harmon. Anal.*, vol. 30, no. 2, pp. 243–261, Mar. 2011.

[22] D. W. Eaton, M. van der Baan, B. Birkelo, and J.-B. Tary, "Scaling relations and spectral characteristics of tensile microseisms: Evidence for opening/closing cracks during hydraulic fracturing," *Geophys. J. Int.*, vol. 196, no. 3, pp. 1844–1857, Mar. 2014.

[23] I. Daubechies, *Ten Lectures on Wavelets*. Philadelphia, PA, USA: SIAM, 1992, ser. CBMS-NSF Regional Conference Series in Applied Mathematics.

[24] G. Thakur, E. Brevdo, N. S. Fučkar, and H.-T. Wu, "The synchrosqueezing algorithm for time-varying spectral analysis: Robustness properties and new paleoclimate applications," *Signal Process.*, vol. 93, no. 5, pp. 1079–1094, May 2013.

[25] M. Van der Baan, D. Eaton, and M. Dusseault, "Microseismic monitoring developments in hydraulic fracture stimulation," in *Effective and Sustainable Hydraulic Fracturing*, R. Jeffrey, Ed. Rijeka, Croatia: InTech, 2013, pp. 439–466.

[26] A. Jurkevics, "Polarization analysis of three-component array data," *Bull. Seismol. Soc. Amer.*, vol. 78, no. 5, pp. 1725–1743, Oct. 1988.

[27] K. Aki and P. Richards, *Quantitative Seismology*. Sausalito, CA, USA: University Science Books, 2002, ser. Geology (University Science Books).: Seismology.

[28] S. Stein and M. Wysession, *An Introduction to Seismology, Earthquakes, Earth Structure*. Hoboken, NJ, USA: Wiley, 2003.

[29] J. Morlet, G. Arens, E. Fourgeau, and D. Giard, "Wave propagation and sampling theory—Part II: Sampling theory and complex waves," *Geophysics*, vol. 47, no. 2, pp. 222–236, Feb. 1982.

[30] M. S. Sams, J. P. Neep, M. H. Worthington, and M. S. King, "The measurement of velocity dispersion and frequency-dependent intrinsic attenuation in sedimentary rocks," *Geophysics*, vol. 62, no. 5, pp. 1456–1464, Oct. 1997.

[31] M. Van der Baan, "Acoustic wave propagation in one-dimensional random media: The wave localization approach," *Geophys. J. Int.*, vol. 145, no. 3, pp. 631–646, Jun. 2001.

[32] Y. Vaezi and M. van der Baan, "Analysis of instrument self-noise and microseismic event detection using power spectral density estimates," *Geophys. J. Int.*, vol. 197, no. 2, pp. 1076–1089, May 2014.

[33] B. Birkelo *et al.*, "High-quality surface microseismic data illuminates fracture treatments: A case study in the Montney," *Leading Edge*, vol. 31, no. 11, pp. 1318–1325, Nov. 2012.

[34] A. Baig and T. Urbancic, "Microseismic moment tensors: A path to understanding frac growth," *Leading Edge*, vol. 29, no. 3, pp. 320–324, Mar. 2010.

[35] N. E. Huang *et al.*, "The empirical mode decomposition and the Hilbert spectrum for nonlinear and non-stationary time series analysis," *Proc. R. Soc. Lond. A, Math. Phys. Sci.*, vol. 454, no. 1971, pp. 903–995, Mar. 1998.

[36] J. Han and M. Van der Baan, "Empirical mode decomposition for seismic time-frequency analysis," *Geophysics*, vol. 78, no. 2, pp. O9–O19, Mar. 2013.

[37] J. B. Tary, R. H. Herrera, and M. Van der Baan, "Time-varying autoregressive model for spectral analysis of microseismic experiments and long-period volcanic events," *Geophys. J. Int.*, vol. 196, no. 1, pp. 600–611, Jan. 2014.